Research Square

Preprints are preliminary reports that have not undergone peer review.
They should not be considered conclusive, used to inform clinical practice,
or referenced by the media as validated information.

Raman Spectroscopic Identification of Biochemical Alterations in Alzheimer's Disease Brain Tissue

Samaneh Ghazanfarpour
University at Albany, State University of New York
Rahul Kumar Das
University at Buffalo, State University of New York
Ivanna Ihnatovych
University at Buffalo, State University of New York
Norbert Sule
Roswell Park Comprehensive Cancer Center
Anna Sharikova
University at Albany, State University of New York
Ravikumar Aalinkeel
University at Buffalo, State University of New York
Alexander Khmaladze
University at Albany, State University of New York
Kinga Szigeti
University at Buffalo, State University of New York
Supriya D. Mahajan
smahajan@buffalo.edu

University at Buffalo, State University of New York

Research Article

Keywords: Raman spectroscopy (RS), Singular Value Decomposition (SVD) , Alzheimer's disease (AD), Neurodegeneration, Cognitive decline, Neuroinflammation, Spectroscopic fingerprints, Protein misfolding, Lipid dysregulation

Posted Date: March 31st, 2026

DOI: https://doi.org/10.21203/rs.3.rs-8844737/v1

License: This work is licensed under a Creative Commons Attribution 4.0 International License.
Read Full License

Additional Declarations: No competing interests reported.

Abstract

Alzheimer's disease (AD) is a progressive neurodegenerative disorder marked by chronic inflammation, neuronal loss, and continuous decline in memory and cognitive function. Raman Spectroscopy (RS) offers a powerful, label-free approach for detecting early biochemical alterations in AD by generating highly sensitive molecular fingerprints. This capability is particularly valuable for identifying subtle changes associated with protein misfolding, lipid dysregulation, and oxidative stress, key processes underlying AD onset and progression. In our study, full-spectrum RS revealed clear biochemical distinctions between control and AD brain tissues, as well as between Braak IV and Braak VI AD stages. Multivariate analytical methods, including Singular Value Decomposition (SVD) and Linear Discriminant Analysis (LDA), were applied to manage spectral complexity and highlight the principal biochemical contributors to AD pathology. Several Raman bands showed increased intensity in AD samples, such as 445 cm^{-1} (N–C–S/C–C skeletal modes), 481 cm^{-1} (DNA phosphate stretching), 560 cm-1 (Glycogen, tyrosine); 690 -780 cm-1 (Nucleic Acids); 748 cm^{-1} (DNA bending), 1080 cm-1 (DNA symmetric stretching vibrations in Phosphate bonds (PO)4-2); 1554 cm^{-1} (Amide II), and 1585 cm^{-1} (protein-folding–related vibrations) and 1607 cm-1 (Aromatic Amino acids- Phenylalanine/tyrosine; Cell Senescence - necrosis marker). These increases indicate enhanced protein aggregation, nucleic-acid structural changes, and backbone reorganization. Conversely, multiple bands decreased in AD tissue, including 880 cm^{-1} (tryptophan deformation), 951–952 cm^{-1} (CH_3 vibrations of α-helical proteins), 1000 cm^{-1} (phenylalanine), 1296 cm^{-1} (lipid CH_2 deformation), 1440 cm^{-1} (lipid/cholesterol deformation), 1640–1680 cm^{-1} (Amide I), and 1732 cm^{-1} (C=O stretching). These reductions reflect loss of ordered protein secondary structure, disruption of aromatic amino-acid environments, and extensive lipid membrane disorganization. Complementary gene-expression analysis further demonstrated dysregulation of lipid homeostasis in AD, with altered expression of ABCA1, LIPE, CPT1A, PPARA, and SREBP-1, indicating broad metabolic reprogramming. Together, the coordinated spectral and transcriptional shifts underscore lipid-metabolic dysfunction as a central feature of AD. By capturing these molecular signatures, RS provides a promising tool for early detection and monitoring of AD progression.

INTRODUCTION

Alzheimer's disease (AD) is the most common cause of dementia and is defined by progressive cognitive decline accompanied by amyloid-β plaques and neurofibrillary tau tangles [1–2]. Despite extensive research, early diagnosis and accurate prognosis remain difficult due to the disease's heterogeneity, variable progression, and complex molecular and genetic influences [3–6]. AD pathology evolves through the spatiotemporal spread of tau, leading to synaptic dysfunction and neuronal loss [7–10]. Although recent therapeutic advances offer modest benefits, AD remains incurable, and early detection is essential for effective intervention. Current diagnostic frameworks rely on biomarkers of β-amyloid and tau deposition, metabolic impairment, and structural atrophy, typically assessed through imaging and cognitive evaluation [1–2]. However, precisely characterizing the density, distribution, and biochemical state of these pathological proteins remains challenging.

Neuropathological staging systems, such as Braak scores, provide a framework for assessing the distribution and severity of tau pathology across brain regions. Braak staging provides a neuropathologically grounded framework that reflects the anatomical spread and biochemical maturation of neurofibrillary tau pathology and correlates closely with clinical disease severity [7–10]. Among these stages, Braak IV and Braak VI represent distinct biological phases that illuminate key transitions in AD progression [11–14]. Braak IV marks a pivotal point at which tau pathology extends into association cortices and symptoms often progress from mild cognitive impairment to early dementia. This stage is defined by emerging hyperphosphorylated tau oligomers, early β-sheet formation, subtle membrane and lipid alterations, mitochondrial stress, and rising oxidative burden, changes that precede major neuronal loss and may still be partially reversible [13–14]. In contrast, Braak VI reflects end-stage disease, characterized by widespread neocortical tau deposition, extensive synaptic and neuronal degeneration, severe mitochondrial failure, chronic inflammation, and collapse of proteostatic and lipid regulatory systems [14]. Tau aggregates at this stage are dominated by insoluble, highly ordered fibrils accompanied by profound lipid depletion, protein oxidation, and activation of cell-death pathways [11–15]. These features represent consolidated, largely irreversible molecular signatures corresponding to severe dementia and minimal therapeutic responsiveness. Thus, Braak IV and Braak VI represent biologically and clinically distinct phases of disease onset and progression, making their comparison particularly informative for understanding AD pathogenesis and identifying opportunities for early detection and therapeutic intervention [7–10]. While Braak staging correlates with disease progression, it is limited in its ability to capture the biochemical heterogeneity that influences individual trajectories of cognitive decline [11–16]. Similarly, genetic risk factors such as the APOE ε4 allele is strongly associated with increased susceptibility to AD and accelerated pathology [17]. However, APOE genotype alone does not fully explain variability in disease onset or prognosis, underscoring the need for complementary approaches that can resolve molecular complexity at the cellular and tissue level. Traditional diagnostic modalities, including neuroimaging and cerebrospinal fluid assays, provide valuable insights but are often invasive, costly, or insufficiently sensitive to detect subtle biochemical changes in the earliest stages of AD [18–20]. This gap highlights the urgent need for label-free, nonperturbative techniques capable of probing molecular alterations directly within biological specimens. AD brain tissue serves as a controlled system to identify AD-related molecular signatures and evaluate the sensitivity of Raman spectroscopy to early biochemical changes. These foundational insights are essential for future translation to accessible biofluids such as blood, where Raman-based assays could ultimately have diagnostic value.

Raman spectroscopy (RS) has emerged as a powerful tool for studying Alzheimer's disease (AD), offering label-free biochemical insights at the molecular level [22]. Unlike conventional methods that rely on exogenous probes, RS enables direct interrogation of brain tissue and cellular specimens while fully preserving their structural, functional, and physiological integrity [23]. As a vibrational spectroscopic technique, RS generates unique biochemical fingerprints from Raman-active biomolecules, enabling detection of subtle molecular shifts associated with protein misfolding, lipid dysregulation, and oxidative stress, which are processes intimately linked to AD onset and progression [23–25]. By applying

multivariate calibration and classification strategies such as Singular Value Decomposition (SVD) and Linear Discriminant Analysis (LDA), RS can disentangle complex spectral datasets, revealing principal biochemical factors that drive variability across heterogeneous brain tissues [25–26]. Our Raman spectroscopic analysis revealed distinct biochemical differences between control and Alzheimer's disease (AD) brain tissues across protein, lipid, carbohydrate, and nucleic-acid vibrational regions.

Integrating RS into AD research may therefore bridge critical gaps between neuropathological staging, genetic risk stratification, and molecular diagnostics. Specifically, RS holds promise for refining the interpretation of Braak scores, and improving prognostic accuracy by capturing biochemical signatures that precede overt clinical symptoms. RS holds promise for refining the interpretation of Braak scores by adding a molecular dimension to a staging system that is currently based solely on the anatomical spread of tau pathology. By revealing molecular heterogeneity within the same Braak stage, identifying subtle biochemical transitions between stages, and detecting early pathological changes before overt tangle formation, RS can provide a more nuanced understanding of disease progression. This molecular resolution has the potential to strengthen the biological meaning of Braak scores and improve their alignment with clinical outcomes.

Such advances could pave the way for earlier intervention strategies, personalized therapeutic approaches, and more precise monitoring of disease progression. Improving the accuracy and timeliness of AD diagnosis is essential for effective intervention and management. Reliable biomarker detection not only facilitates early identification of the disease but also aids in monitoring progression and evaluating therapeutic outcomes. Several recent studies have demonstrated the feasibility of applying RS to blood, plasma, serum, and peripheral cells, suggesting that Raman-derived molecular markers identified in brain tissue may ultimately be detectable in minimally invasive samples [27–28]. Although, our current work uses brain tissue as a discovery platform, the long-term clinical translational potential of our work includes blood-based or other peripheral Raman assays, which could complement existing biomarkers and address the need for label-free, nonperturbative, and cost-effective diagnostic tools. As the global prevalence of AD continues to rise, enhancing diagnostic methodologies will play a critical role in reducing the economic and emotional burden on patients, families, and healthcare systems. Ultimately, RS offers a noninvasive, highly sensitive diagnostic modality that holds promise for identifying early-stage Alzheimer's disease and monitoring its progression, paving the way for improved therapeutic interventions and patient outcomes.

MATERIALS AND METHODS

Sample Collection and Preparation

The study sample was composed of post mortem tissue samples obtained from AD patients who were diagnosed based on NINCDS-ADRDA criteria and were obtained from the archived tissue bank from Baylor. The inclusion criteria for AD samples were (1) age ≥ 50 years old, (2) access to neuropsychological and clinical data. The exclusion criteria included (1) history of psychiatric and major

depressive disorder prior to the onset of AD. Inclusion and exclusion criteria for Control samples were (1) ≥ 50 years old, (2) no history of neurological or medical illness that might impact cognitive function, and (5) no diagnosis of major depressive disorder. The study was approved by the Institutional Review Board (IRB) and all protocols were approved by the Ethics Committee of the Jacobs School of Medicine and Biomedical Sciences, Buffalo, NY, USA. The demographic and clinical information of the samples are shown in Table I.

TABLE I: Demographic and Clinical information of the samples

Brain Bank	Design ID	Diagnosis	APO_E	SEX	Age at death (cal)	Frozen PMI	Plaque score (0 = none, 1 = sparse, 2 = moderate, 3 = dense)	Braak stage (0–6)
Baylor	3	AD		F	78	24 hours	CERAD C	VI
Baylor	15	AD	3,4	F	76	9.5 hours	CERAD C	IV
NYBB	T-139	NC		M	57	N/A		
NYBB	T-638	NC		M	78	5.5 hours		

Raman Spectra Acquisition of AD brain tissue

Paraffin-embedded sections (4 μm) of the AD and Control samples (n = 2/ group) were obtained and were used for the Raman spectral analysis. The parafilm peaks were eliminated by software-guided subtraction of the Raman spectra of standard parafilm from the acquired spectral data of samples. No staining or chemical treatment was applied to enable preservation of the native biochemical composition of the tissue for Raman analysis. Scattered Raman light from a laser beam focused on a tissue section provided detailed information about the molecular composition of the tissue at the microscopic level. Multiple spectra were obtained per tissue section to account for heterogeneity.

Raman spectra were acquired by a commercial Raman micro-spectroscope (HORIBA XploRA PLUS) equipped with a 1024×256 TE air-cooled CCD chip (pixel size 26 μm, temperature − 60°C). Spectra were acquired using a 532 nm laser operating at a power of 0.065 W, with an 1800 grooves/mm grating, a slit width of 100 μm, and a pinhole diameter of 100 μm. Each spectrum was recorded with an acquisition time of 30 seconds and three accumulations to enhance signal quality. A 40x objective was employed for focusing, and a total of 100 spectra per sample were collected for analysis. Spectra were acquired over 200–2000cm^{-1} (fingerprint region).

Raman Data Processing and Analysis

HORIBA LabSpec6 software was used for the initial data processing: smoothing, baseline removal (polynomial), and normalization (unit vector), necessary to enable subsequent quantitative analysis [25–29]. SVD analysis of the spectra was done using Python code to obtain the critical spectral features differentiating between the tissue samples. All Raman spectra from each imaging dataset were aggregated to form an input matrix for the SVD algorithm. In particular, the Raman spectra acquired from individual points within each sample were organized to generate a matrix of size m × n, where m denotes the number of data points per spectrum, and n indicates the total number of spectra within a specific sample [30–33]. In our study, these dimensions were 1116 X 200. Subsequently, we applied the SVD function in Python to decompose the input matrix into matrices U, Σ, and V^T. The matrix V was utilized to create SVD scatter plots, whereas the individual SVD components were stored in the matrix U [34–36].

Each scatter plot was based on the leading SVD components and contained two data sets, AD's vs. controls, or between the two AD samples belonging to the Braak stage IV vs Braak stage VI, where each spectrum was represented as a single point. A separating line was constructed using Linear Discriminant Analysis (LDA), a supervised classification technique that identifies the linear combination of features which maximizes the separation between classes by maximizing the distance between their means while minimizing the variance within each class [36–37]. A corresponding confusion matrix, summarizing the classification performance for each sample, was also generated. Additionally, the SVD components employed in the scatter plots, each of which contained the spectral features responsible for distinguishing the datasets, were plotted.

Statistical Analysis

Statistical analysis was done using GraphPad Prism (v8; GraphPad Software, Boston, MA). The comparison between the AD samples vs. controls, or between the two AD samples belonging to the Braak stage IV vs Braak stage VI, was done using a non-parametric test Mann–Whitney U test (Wilcoxon rank-sum test). All statistical analyses were performed using non-parametric methods due to the small sample size and the inability to assume normal distribution of the data. A two-tailed p-value < 0.05 was considered statistically significant.

For Raman analysis, Singular Value Decomposition (SVD) was used solely for visualization purposes, not for classification or model fitting [37–38]. This approach inherently avoids overfitting, as SVD was not part of the predictive pipeline. We selected the first six components based on their cumulative explained variance, which captured the most informative structure in the data while minimizing noise. Linear Discriminant Analysis (LDA) was applied for classification, and we ensured robustness by performing cross-validation during model evaluation. This helped assess generalizability and mitigate overfitting risks. The following flowchart represents our steps:

BODIPY™ 581/591 C11 Lipid Peroxidation Sensor:

Paraffin-embedded brain tissue sections (4 μm) were obtained from clinically and neuropathologically confirmed Alzheimer's disease (AD) cases (n = 2) and age-matched non-demented controls (n = 2). Sections were briefly equilibrated to room temperature deparaffinized and lightly fixed in 4% paraformaldehyde for 5 min to preserve morphology while maintaining lipid integrity, followed by washing in PBS. Lipid peroxidation was assessed using the BODIPY™ 581/591 C11 Lipid Peroxidation Sensor (Thermo Fisher Scientific), prepared fresh at 2 μM in PBS containing 0.05% fatty-acid–free BSA. Sections were incubated with the probe for 30 min at 37°C in a humidified, light-protected chamber, washed three times in PBS, counterstained with DAPI when required, and mounted in aqueous antifade medium. Fluorescence imaging was done using the Revolve Discover ECHO microscope using identical acquisition settings across all samples, with oxidized probe (green) detected using 488-nm excitation/500–550-nm emission and the reduced form (red) using 561-nm excitation/580–620-nm emission. For each case, multiple non-overlapping fields were imaged and analyzed in Fiji/ImageJ. Mean fluorescence intensities for oxidized (green) and reduced (red) channels were background-subtracted, and lipid peroxidation was quantified as the green-to-red fluorescence ratio for each region. Values from all fields were averaged to generate one per-case measurement, enabling descriptive comparison between AD and control groups.

Gene expression analysis from human brain tissue:

Brain tissue samples were obtained from clinically and neuropathologically confirmed Alzheimer's disease (AD) patients and age- and sex-matched non-demented controls (n = 10 per group. Samples from AD patients who were diagnosed based on NINCDS-ADRDA criteria and were obtained from the archived tissue bank from Baylor. Tissue blocks (~ 50–100 mg) were dissected from the same anatomical region (Pre-frontal cortex) to minimize regional variability. Samples were snap-frozen in liquid nitrogen immediately after collection and stored at − 80°C until RNA extraction

RNA Extraction:

RNA was extracted from brain tissue samples using the TRIzol® reagent (Invitrogen-Life Technologies, Carlsbad, CA). The amount of RNA was quantified using a NanoDrop ND-1000 spectrophotometer (Nano-Drop™, Wilmington, DE), and isolated RNA was stored at -80°C until it was used.

Real-Time Quantitative (RT-q) PCR:

Total RNA (1000 ng) that was extracted as described above was utilized for the All-in-One Universal RT cDNA Master Mix Synthesis Kit (Lamba Biotech, St. Louis, MO, Cat #G209) following the Manufacturer's protocol. One microliter of the resultant cDNA from the RT reaction was employed as the template in PCR reactions using well-validated PCR primers for IL-6, TNF-α, GPX-1, ABCA1, LIPE, CPT1A, PPARA, and SREBP-1 obtained from RealTimePrimers.com; and the final primer concentration used in the PCR was 0.1 μM. We used the SYBR® Green master (Bio-Rad, Hercules, CA) following the Manufacturer's QPCR

protocol, and gene expression was calculated using the comparative CT method. The threshold cycle (Ct) of each sample was determined, and β-actin was used as the endogenous reference gene. The relative level of a transcript (2ΔCt) was calculated by obtaining ΔCt (test Ct − β-actin Ct), and transcript accumulation index (TAI) was calculated as TAI = $2^{-\Delta\Delta CT}$ [39–40]

RESULTS

Raman Spectral Analysis:

Raman spectroscopic analysis revealed distinct biochemical differences between control and Alzheimer's disease (AD) brain tissues and between Braack IV and Braack VI AD stages. The following is a detailed description of the Raman spectral variation between AD samples vs controls. Raman spectroscopic analysis revealed distinct biochemical differences between control and Alzheimer's disease (AD) brain tissues across the 445–1732 cm^{-1} region (Fig. 1 [c-f]) and Table 1). AD samples exhibited significant increases in low-frequency vibrational modes at 445, 481, and 748 cm^{-1}, reflecting altered protein–carbohydrate environments and pronounced perturbations in nucleic-acid backbone structure consistent with DNA fragmentation and inflammatory activity. In contrast, several protein- and lipid-associated bands showed marked reductions in AD tissue. [41–44]. Decreases at 880, 951–952, and 1000 cm^{-1} indicated disruption of aromatic amino-acid environments and loss of ordered α-helical content, while diminished intensities at 1296 and 1440 cm^{-1} pointed to compromised lipid-chain organization and membrane structural integrity [45]. Protein backbone alterations were further supported by increased Amide II (1554 cm^{-1}) and 1585 cm^{-1} aromatic-backbone modes, accompanied by a pronounced reduction in the Amide I region (1640–1680 cm^{-1}), signifying broad secondary-structure destabilization [46–48]. A decrease in the 1732 cm^{-1} carbonyl band suggested additional alterations in steroid- and lipid-derived carbonyl species. Also, an enhanced signal at 560 cm^{-1}, corresponding to glycogen and tyrosine-related skeletal modes, was observed in AD samples, suggesting altered carbohydrate storage and amino-acid microenvironments. A broad increase in the 690–780 cm^{-1} region, associated with nucleic-acid vibrations, indicated elevated contributions from DNA/RNA structural components [47–49]. AD tissue also exhibited a marked rise in the 1080 cm^{-1} band, representing symmetric phosphate stretching of DNA (PO_4^{2-}), consistent with nucleic-acid backbone perturbation and the 1607 cm^{-1} band is linked to aromatic amino acids such as phenylalanine and tyrosine and often associated with protein senescence or necrotic processes, also showed pronounced elevation in AD samples [50]. Together, these spectral increases highlight distinct biochemical alterations in AD brain tissue across carbohydrate, nucleic-acid, and protein-related vibrational domains. Collectively, these spectral changes indicate coordinated disruptions in nucleic acids, proteins, and lipids that characterize AD-associated molecular pathology [49–51].

Table 1
Raman Spectral Bands and their Biochemical Structural Assignment

Raman Band (1/cm)	Intensity Change (Control vs AD)	Biological Relevance
445	*Increase*	*N-C-S stretch in proteins and C-C bond stretch in carbohydrates*
481	*Increase*	*DNA stretching vibrations in phosphate bonds (PO)4 2-*
560	*Increase*	*Glycogen, tyrosine*
690–780	*Increase*	*Nucleic Acid band*
748	*Increase*	*DNA bending vibration*
880	*Decrease*	*Tryptophan, δ (ring) disorentation*
951	*Decrease*	*ν(CH_3) of proteins (α-helix) foldings*
1000	*Decrease*	*Phenylalanine ring resonance*
1080	*Increase*	*DNA symmetric stretching vibrations in Phosphate bonds $(PO)_4^{-2}$*
1296	*Decrease*	*CH_2 deformation in lipid aliphatic chains*
1440	*Decrease*	*CH_2 and CH_3 deformation vibrations* *CH deformation, Cholesterol, fatty acid band, δ (CH_2) (lipids)*
1554	*Increase*	*Amide II band in proteins*
1585	*Increase*	*Protein folding assignment*
1607	*Increase*	*Aromatic Amino acids (Phenylalanine/tyrosine) Cell Senescence- necrosis marker*
1640–1680	*Decrease*	*Amide I in protein band*
1732	*Decrease*	*One of absorption positions for the C = O stretching vibrations of cortisone*

A heatmap depicting the distribution range of Raman spectral bands (560–1730 cm^{-1}) under three experimental conditions: Control, Braack IV, and Braack VI are shown in Fig. 1f. Analysis of the Raman spectral distribution revealed condition-dependent variability across several key vibrational bands. Control samples exhibited consistently low distribution ranges across the spectrum, suggesting molecular homogeneity. In contrast, Braack IV samples showed moderate increases in variability, particularly at 720 cm^{-1}, 960 cm^{-1}, and 1440 cm^{-1}, indicating early biochemical alterations. Braack VI

samples demonstrated the highest distribution ranges, with pronounced variability in bands near 720 cm^{-1}, 960 cm^{-1}, 1240 cm^{-1}, and 1440 cm^{-1}. These shifts suggest extensive molecular changes associated with advanced neurodegenerative pathology [52–53]. Panel I shows Clear separation between the control AD groups is observed, indicating that all SVD components effectively capture the variance in the data. Fractions of explained variance in Control sample and Braak IV are 0.636 (SVD1) and 0.035 (SVD2), and 0.623 (SVD1) and 0.055 (SVD2) for Control sample and Braak VI and 0.612 (SVD1) and 0.057 (SVD2) for Braak IV and Braak VI samples (Fig. 2 [a-l]). Separator lines generated by LDA show the boundaries between the Control region and each AD group and between Braak IV and Braak VI. Panel II shows confusion matrices, demonstrating classification performance using all SVD components for comparisons between controls and each AD group and between Braak IV and Braak VI respectively, showing, with 65 out of 100 for control samples and all 55 for Braak IV (Fig. 2b) and 98 out of 100 for control samples and 99 for Braak VI AD samples (Fig. 2f) and 98 out of 100 for control samples and 99 out of 100 for Braak VI AD samples and 90 for Braak VI (Fig. 2j). Panel III shows Receiver operating characteristic (ROC) curve analysis confirmed the classification performance between control and each AD group and between Braak IV and Braak VI samples yielding an accuracy of 0.60, precision of 0.611, and an F1 score of 0.579 for the control vs Braak IV samples (Fig. 2c) and an accuracy of 0.985, precision of 0.980, and an F1 score of 0.985 for the control vs Braak VI samples (Fig. 2g) and an accuracy of 0.945, precision of 0.989, and an F1 score of 0.942 for the Braak IV vs Braak VI samples respectively (Fig. 2k). Panel IV outlines spectral differentiation across samples showing comparative signal shifts between control vs Braak IV samples (Fig. 2d); control vs Braak VI samples (Fig. 2h) and Braak IV vs Braak VI samples (Fig. 2l) respectively.

Analysis of gene expression in age and sex matched post-mortem brain tissue revealed substantial alterations in pathways related to lipid metabolism, inflammation, and oxidative stress in Alzheimer's disease (AD). Quantitative PCR measurements demonstrated marked dysregulation of genes involved in lipid breakdown, fatty-acid oxidation, and lipid synthesis, as well as key inflammatory cytokines and the antioxidant enzyme GPX1.

Expression of LIPE, a critical lipolytic enzyme, was reduced by 91% in AD samples compared with controls (TAI = 0.09 ± 0.012; $p < 0.0001$). Similarly, the lipid transporter ABCA1 showed a 78% decrease (TAI = 0.22 ± 0.11; $p < 0.01$), and PPARA, a regulator of fatty-acid oxidation, was reduced by 83% (TAI = 0.17 ± 0.05; $p < 0.0001$). Expression of GPX1, which encodes the antioxidant enzyme glutathione peroxidase-1, was also significantly diminished, showing a 73% decrease in AD tissue (TAI = 0.27 ± 0.03; $p < 0.001$).

Genes associated with lipid synthesis and fatty-acid oxidation were upregulated. SREBP-1 expression increased by 46% (TAI = 1.46 ± 0.13; $p < 0.05$), and CPT1A, a key enzyme in mitochondrial fatty-acid transport, increased by 62% (TAI = 1.62 ± 0.07; $p < 0.01$). Markers of neuroinflammation were also elevated. TNF-α expression was 59% higher in AD samples (TAI = 1.59 ± 0.089; $p < 0.01$), and IL-6 expression increased by 61% (TAI = 1.61 ± 0.071; $p < 0.01$).

Together, these findings indicate a coordinated disruption of lipid metabolic pathways, heightened inflammatory signaling, and reduced antioxidant capacity in AD brain tissue.

Lipid peroxidation, assessed using the BODIPY™ 581/591 C11 probe, was markedly elevated in Alzheimer's disease (AD) brain tissue compared with age-matched controls. AD sections exhibited a pronounced shift from reduced (red) to oxidized (green) fluorescence, indicating increased peroxidation of lipid droplets, whereas control samples showed predominantly red signal (Fig. 3m). Quantification of green-to-red fluorescence ratios confirmed consistently higher lipid oxidation in AD cases. Stratification by neuropathological stage revealed a clear progression of oxidative damage: Braak IV tissue showed a 22% increase ($p < 0.05$) in lipid peroxidation relative to control, while Braak VI tissue demonstrated a substantially greater 80% increase ($p < 0.01$), accompanied by more extensive punctate green aggregates throughout affected cortical regions. These findings, illustrated in Fig. 3n, highlight a stage-dependent escalation in lipid peroxidation and lipid aggregation with advancing tau pathology, supporting a link between oxidative lipid damage and late-stage AD neurodegeneration.

DISCUSSION

Alzheimer's disease involves a constellation of interconnected patho-mechanisms, which include amyloid-β aggregation, tau misfolding and fibrillization, oxidative stress, lipid membrane disruption, mitochondrial dysfunction, and progressive synaptic degeneration, all of which collectively drive neurodegeneration [54–58]. Each of these processes produces distinct biochemical alterations in proteins, lipids, and nucleic acids, many of which manifest as changes in molecular structure, bond vibrations, and chemical composition. Raman spectroscopy (RS), with its sensitivity to protein secondary structure, β-sheet enrichment, lipid saturation and degradation, oxidative modifications, and metabolic shifts, is uniquely positioned to detect these molecular signatures directly within tissue. In recent years, Raman spectroscopy (RS) has emerged as a promising, non-invasive analytical technique for the detection of AD-related biochemical changes [59]. In our study, Raman spectroscopic analysis revealed clear biochemical distinctions between control and Alzheimer's disease (AD) brain tissues and between Braak IV and Braak VI AD stages, across multiple spectral regions. Several low-frequency vibrational bands showed consistent increases in intensity in AD samples, indicating structural and molecular alterations associated with neurodegeneration. These Raman-derived biochemical fingerprints align closely with known AD mechanisms, demonstrating that RS not only detects but also differentiates key pathological processes, thereby validating its utility as a molecularly resolved tool for probing AD progression. Raman-derived biochemical signatures at Braak IV reflect early, heterogeneous, and potentially modifiable disease processes, whereas Braak VI spectra capture the stabilized molecular fingerprint of end-stage neurodegeneration. These features make Raman spectroscopy particularly powerful for identifying early disease-associated biochemical patterns that are obscured or lost at later stages.

A marked increase at 445 cm^{-1} was observed in AD tissues, reflecting enhanced N–C–S bending and C–S stretching in proteins, along with C–C skeletal vibrations from carbohydrates. This heightened signal

suggests altered environments around sulfur-containing amino acids, changes in disulfide bonding, and increased rigidity within aggregated proteins such as amyloid-β and hyperphosphorylated tau, both of which contain sulfur-bearing amino acids whose local environments shift during misfolding and fibrillization [60]. The contribution from carbohydrate-related modes also points to disrupted glucose metabolism and glycan processing, indicating broader biochemical remodeling in plaque- and tangle rich regions [60].

The 481 cm^{-1} band likewise showed elevated intensity in AD samples. This feature, linked to symmetric phosphate stretching in DNA, suggests changes in nucleic acid structure or abundance, potentially due to DNA fragmentation, chromatin alterations, or extracellular DNA associated with inflammation and degeneration [41–48]. Together, the enhanced 445 cm^{-1} and 481 cm^{-1} Raman signals highlight protein, carbohydrate, and nucleic-acid-related molecular alterations in AD tissue, underscoring Raman spectroscopy's sensitivity to subtle biochemical signatures of neurodegeneration.

The increased intensity of specific Raman bands in AD tissue reflects widespread molecular remodeling characteristic of neurodegeneration. The elevation at 560 cm^{-1} suggests disruptions in glycogen metabolism and altered tyrosine-containing protein structures, both of which have been implicated in impaired neuronal energy homeostasis and oxidative stress responses in AD. Enhanced nucleic-acid–related signals in the 690–780 cm^{-1} region, together with the strengthened 1080 cm^{-1} phosphate band, point toward DNA/RNA structural instability, chromatin remodeling, or increased nucleic-acid fragmentation, which are features commonly associated with neuroinflammation, oxidative damage, and impaired genomic maintenance in AD neurons [41–48].

The 748 cm^{-1} band also showed a clear increase in AD tissue, reflecting DNA bending and deformation modes. This enhancement supports the presence of nucleic-acid structural alterations associated with AD, including genomic instability, oxidative DNA damage, and nucleic-acid release during cell death. The elevated signal likely reflects DNA conformational stress, fragmentation, or changes in chromatin compaction [61–64]. Together with other spectral shifts, this increase highlights Raman spectroscopy's sensitivity to nucleic-acid remodeling in AD.

A notable decrease was observed at 880 cm^{-1} in AD samples. This band, linked to tryptophan vibrations, is highly sensitive to protein tertiary structure and its reduction suggests increased protein disorder, misfolding, and aggregation, which are hallmarks of amyloid-β and tau pathology, as well as possible oxidative modification of aromatic residues [64–68].

Similarly, the 951–952 cm^{-1} band decreased in AD tissue, consistent with α-helix destabilization and the transition of proteins toward β-sheet-rich, aggregated states. Oxidative stress and proteolytic activity in AD may further diminish this CH_3 vibrational signature [61–67].

Overall, the combined increases at 445, 481, and 748 cm^{-1} and decreases at 880 and 951–952 cm^{-1} reflect coordinated biochemical remodeling of proteins, carbohydrates, and nucleic acids in AD brain

tissue, underscoring Raman spectroscopy's utility for detecting molecular signatures of Alzheimer's pathology.

The 1000 cm^{-1} band, corresponding to phenylalanine ring-breathing, showed reduced intensity in AD tissue. This decrease reflects disruptions in aromatic amino-acid environments and is consistent with widespread protein misfolding, β-sheet–rich aggregation of amyloid-β and tau, and oxidative or proteolytic damage [61–68].

The 1296 cm^{-1} band also decreased in AD samples. This CH_2 deformation mode reports on lipid-chain organization, and its attenuation aligns with AD-related membrane degradation, altered phospholipid composition, and oxidative lipid damage, indicating broader disruption of membrane structure [69].

A similar reduction occurred at 1440 cm^{-1}, a region dominated by CH_2/CH_3 deformation vibrations from lipids, cholesterol, and fatty-acid chains. The diminished signal reflects impaired membrane integrity and lipid homeostasis, reinforcing the extensive lipid dysregulation characteristic of AD [69].

In contrast, the 1554 cm^{-1} Amide II band increased in AD tissue. This enhancement reflects altered N–H bending and C–N stretching associated with protein backbone reorganization during amyloid-β and tau aggregation, as well as additional structural modifications driven by inflammation and oxidative stress [46–48].

The 1585 cm^{-1} band likewise increased, indicating changes in aromatic-ring and backbone vibrations linked to protein folding and higher-order structural transitions. This rise is consistent with β-sheet–rich fibril formation and oxidative modification of protein assemblies [66].

Together, these spectral changes, decreases in lipid- and aromatic-related bands and increases in protein-backbone modes, highlight coordinated disruptions in protein structure, lipid organization, and overall biochemical architecture in AD brain tissue.

The pronounced increase at 1607 cm^{-1}, representing aromatic amino-acid vibrations and linked to protein senescence and necrotic pathways, further supports the presence of advanced protein damage and aggregation. This aligns with known AD hallmarks, including accumulation of oxidized proteins, misfolded aggregates, and heightened cellular stress responses [61–68]. The combined elevation of these Raman features underscores the multifactorial biochemical deterioration occurring in AD brain tissue, reflecting converging disruptions in energy metabolism, nucleic-acid integrity, and protein homeostasis.

The 1640–1680 cm^{-1} region, corresponding to the Amide I band, showed reduced intensity in AD tissue. Because this band reflects C = O stretching and is highly sensitive to protein secondary structure, its attenuation indicates destabilization of α-helical and β-sheet content. This decrease aligns with the extensive protein misfolding and the shift of amyloid-β and tau toward β-sheet-rich fibrillar aggregates, reinforcing evidence of widespread structural disruption in AD [68].

The 1732 cm^{-1} band also decreased in AD samples. This carbonyl-stretching region is associated with cortisone and related steroid structures. Its reduction is consistent with AD-related metabolic dysregulation, including impaired steroidogenesis, altered glucocorticoid signaling, and oxidative modification of lipid and steroid backbones [61–68]. The diminished signal reflects broader disruption of carbonyl-containing molecules and complements the protein, lipid, and nucleic-acid alterations observed across the Raman spectrum.

The comparative analysis of Braak IV and Braak VI brain tissue enabled delineation of biochemical changes that occur early in disease progression from those that represent downstream consequences of irreversible neuronal injury. As depicted in the heat map shown in Fig. 4, the progressive increase in Raman spectral variability from Control to Braack VI reflects escalating biochemical heterogeneity, likely driven by tau-associated neurodegeneration. The bands exhibiting the most pronounced changes such as 720 cm^{-1} (nucleic acid vibrations), 960 cm^{-1} (phosphate backbone), and 1240–1440 cm^{-1} (protein and lipid signatures), are consistent with known molecular disruptions in Alzheimer's disease progression. The elevated distribution range in Braack VI samples suggests widespread molecular disorganization, potentially reflecting synaptic loss, gliosis, and altered lipid metabolism. These findings support the utility of Raman spectroscopy as a sensitive tool for detecting molecular alterations across Braack stages. The spectral bands identified may serve as candidate biomarkers for staging and monitoring disease progression, offering insights into the biochemical landscape of tauopathy.

Identifying molecular features that emerge at Braak IV but intensify or become fixed at Braak VI is essential for defining early biomarkers, therapeutic targets, and mechanistic drivers of AD progression.

From a translational perspective, the ability of Raman spectroscopy to distinguish Braak IV from Braak VI based on intrinsic biochemical signatures supports its potential utility as a platform for early AD detection, disease staging, and therapeutic stratification. By defining spectroscopic markers that precede extensive neuronal loss, this approach may inform the development of diagnostics and interventions aimed at intercepting AD during its most treatable phase.

Alzheimer's disease profoundly disrupts lipid homeostasis. Genes involved in lipid breakdown, fatty-acid oxidation, and lipid synthesis show altered expression in AD brain tissue. Genes ABCA1 (ATP Binding Cassette Subfamily A Member 1), LIPE (Lipase), CPT1A (carnitine palmitoyl transferase 1A enzyme), PPARA (Peroxisome Proliferator-activated receptor-alpha), and SREBP-1 (Sterol Regulatory Element-Binding Protein 1) represent key nodes in this metabolic network [69–75]. We observed modulations of these genes associated with Lipid metabolism in AD brain tissue samples. ABCA1 plays a central role in the brain's response to disrupted lipid metabolism in Alzheimer's disease. As AD progresses, neurons and glial cells accumulate excess free cholesterol, along with elevated levels of oxidized cholesterol derivatives that rise during oxidative stress and neuroinflammation. These lipid disturbances also drive the formation of lipid droplets, a hallmark of metabolic stress in affected brain regions. ABCA1 function is often impaired in AD, and reflects metabolic stress and defective lipid clearance [69]. LIPE, is a major lipase responsible for mobilizing stored triglycerides, showed reduced expression relative to control

tissue, consistent with the lipid droplet accumulation widely reported in AD astrocytes and microglia [71]. CPT1A, is the rate-limiting enzyme for mitochondrial fatty-acid β-oxidation, was found to be upregulated, in AD samples, reflecting a compensatory metabolic shift toward fatty-acid utilization in the context of impaired glucose metabolism [72–73]. This pattern aligns with the broader metabolic reprogramming observed in AD. PPARA, a nuclear receptor that promotes fatty-acid oxidation and suppresses inflammation, exhibited reduced expression in AD samples, suggesting insufficient transcriptional support for lipid clearance pathways [74]. SREBP-1, is believed to be a master regulator of fatty-acid and triglyceride synthesis, and its expression was increased in AD samples, reinforcing that a lipid-anabolic state that may exist that exacerbates lipid droplet formation and metabolic stress [75]. Together, these gene-expression changes point to a coordinated imbalance in lipid synthesis, breakdown, and oxidation, contributing to the metabolic dysfunction that characterizes the Alzheimer's disease brain. We observed reduced GPX1 gene expression in the brains AD patients, which results in increased oxidative stress. Reduced GPX1 activity is associated with cognitive decline, and its deficiency worsens Amyloid beta-induced neurotoxicity [76]. TNF-α and IL-6 are two of the most consistently elevated cytokines in the Alzheimer's disease brain, where they drive the chronic neuroinflammatory environment that accelerates neurodegeneration [77–78]. Activated microglia and astrocytes surrounding amyloid-β plaques release high levels of TNF-α, which in turn activates NF-κB signaling and stimulates the production of inflammatory mediators, like IL-6. This creates a self-reinforcing inflammatory loop that impairs microglial clearance of amyloid-β, increases amyloid precursor protein processing, and promotes tau phosphorylation. Elevated IL-6 further amplifies microglial activation, oxidative stress, and acute-phase responses, contributing to synaptic dysfunction and neuronal loss [77–81]. Both cytokines are found at increased levels in AD brain tissue but also in cerebrospinal fluid and peripheral blood, suggesting that central and systemic inflammation are interconnected in AD [82–84].

Our study demonstrates a clear increase in lipid peroxidation in Alzheimer's disease (AD) brain tissue compared with age-matched controls, as revealed by oxidation-dependent spectral shifts of the BODIPY™ 581/591 C11 probe. The elevated green-to-red fluorescence ratios observed in AD samples support the concept that oxidative damage to membrane lipids is a prominent feature of AD pathology. These findings align with extensive evidence implicating oxidative stress as an early and persistent driver of neurodegeneration, particularly in regions vulnerable to amyloid and tau accumulation. Notably, the greater lipid peroxidation and more pronounced lipid aggregate formation in Braak stage VI compared with Braak stage IV suggests that oxidative membrane injury intensifies with advancing tau pathology. This progression is consistent with models proposing that mitochondrial dysfunction, impaired antioxidant defenses, and iron-dependent lipid oxidation (including ferroptosis-related mechanisms) become increasingly dysregulated in late-stage AD [70–75]. The spatial pattern of punctate oxidized lipid aggregates observed in Braak VI tissue further supports the idea that chronic oxidative stress contributes to membrane destabilization, synaptic vulnerability, and neuronal loss. Although the small sample size limits statistical inference, the consistency of the ratiometric shift across cases underscores the robustness of lipid peroxidation as a pathological marker. Together, these

results reinforce the view that lipid oxidative damage is not merely a byproduct of AD pathology but may actively contribute to disease progression, highlighting the potential value of therapeutic strategies aimed at stabilizing membrane lipids or modulating lipid-oxidation pathways.

Overall, RS provides a molecular fingerprint of biofluids and tissues by measuring vibrational modes of biomolecules, enabling the identification of subtle alterations associated with amyloid-beta and tau proteins, oxidative stress, and lipid peroxidation. Unlike conventional imaging methods, RS offers rapid, label-free analysis and can be enhanced through advanced computational approaches such as machine learning. Integrating RS into AD diagnostics may improve sensitivity and specificity, particularly in the early stages of disease, thereby supporting timely intervention and personalized care strategies. Raman spectroscopy has shown considerable promise in the context of Alzheimer's disease by enabling early detection of subtle biochemical changes in blood and cerebrospinal fluid, often before clinical symptoms become apparent. As the disease progresses, this technique reveals increasingly pronounced signals associated with protein misfolding, lipid peroxidation, and neuroinflammation, providing valuable insights into the underlying pathology. In Alzheimer's disease (AD), protein misfolding, lipid peroxidation, and neuroinflammation represent interconnected pathological processes that evolve across different stages of disease progression. During the preclinical phase, misfolded amyloid-β oligomers and tau seeds begin to accumulate, accompanied by subtle oxidative stress and early microglial activation [80–82]. As patients transition to mild cognitive impairment, amyloid plaques and tau tangles disrupt synaptic function, lipid peroxidation products increase, and microglia release pro-inflammatory cytokines [83–84]. In the early dementia stage, dense amyloid plaques and hyperphosphorylated tau tangles are evident, with oxidative damage to neuronal membranes and mitochondria amplifying neurotoxicity, while astrocytes and microglia sustain inflammatory cascades. Moderate dementia is marked by widespread tau pathology, high levels of lipid peroxidation biomarkers, and chronic neuroinflammation with blood–brain barrier disruption. In severe dementia, extensive neuronal death occurs due to overwhelming protein aggregation, irreversible oxidative damage, and persistent glial activation, culminating in widespread neurodegeneration and functional decline. This stage-wise interplay underscores the importance of targeting these processes collectively for early diagnosis and therapeutic intervention.

Conclusion

The gene-expression profile observed in Alzheimer's disease brain tissue points to a coordinated disruption of lipid homeostasis which reflects a maladaptive metabolic state characterized by excess lipid storage, mitochondrial dysfunction, and heightened neuroinflammation. Such a pattern underscores the central role of lipid-metabolic dysregulation in AD pathophysiology. Overall, the modulation of the Raman spectral signatures in AD samples as compared to controls, reinforces the utility of Raman spectroscopy as a sensitive tool for detecting molecular alterations associated with AD pathology and highlight its potential for identifying early biochemical markers of neurodegeneration. Raman-based biochemical phenotyping provides a valuable bridge between neuropathological staging and molecular mechanism, offering insights into why therapeutic efficacy diminishes as AD advances to late Braak stages. Beyond its diagnostic capabilities, Raman spectroscopy holds significant clinical potential as a

complementary tool to conventional imaging and laboratory tests, offering a faster, non-invasive approach for monitoring disease onset and progression. The present study serves as a mechanistic and exploratory foundation for future development of Raman-based peripheral biomarkers rather than a direct diagnostic comparison to imaging or CSF assays.

Declarations

Author Contributions:

Conceptualization: Alexander Khmaladze, Kinga Szigeti, Supriya D. Mahajan

Investigation: Samaneh Ghazanfarpour, Rahul Kumar Das, Ivanna Ihnatovych

Visualization: Samaneh Ghazanfarpour, Rahul Kumar Das

Supervision: Anna Sharikova, Alexander Khmaladze, Kinga Szigeti, Supriya D. Mahajan

Writing-original draft: Supriya D. Mahajan, Kinga Szigeti

Writing-review and editing: Ravikumar Aalinkeel, Samaneh Ghazanfarpour, Rahul Kumar Das, Alexander Khmaladze, Kinga Szigeti, Norbert Sule, Supriya D. Mahajan

All authors approved the final manuscript.

Ethics approval and consent to participate

The study was approved by the Institutional Review Board (IRB), and all protocols received approval from the Ethics Committee of the Jacobs School of Medicine and Biomedical Sciences, Buffalo, NY, USA. All procedures adhered to established ethical standards for research involving human subjects. Because the study involved analysis of post-mortem brain tissue, the requirement for informed consent was waived by the IRB. All data were handled in compliance with the Health Insurance Portability and Accountability Act (HIPAA). Patient confidentiality was safeguarded through de-identification of all extracted data, secure storage on password-protected institutional servers, and restricted access limited to authorized study personnel. No identifiable personal health information was disclosed or used outside the scope of this research

Consent for Publication

All participants (or their legal guardians, where applicable) provided informed consent for the publication of anonymized clinical information, images, and any accompanying data included in this manuscript. The authors affirm that all identifying details have been removed or anonymized to protect patient privacy. Written consent was obtained in accordance with institutional guidelines and the ethical standards of the Declaration of Helsinki. Documentation of consent is available for review by the Editor of Acta Neurologica Communications upon request.

Competing Interests

The authors declare that they have no competing interests related to this work.

Funding

No external funding was received to support this study. All research activities were conducted without financial sponsorship from public, commercial, or nonprofit funding agencies.

Acknowledgements

This study was made possible in part by Alzheimer Association AARG-16–443615, Edward A. and Stephanie E. Fial Fund, Community Foundation for Greater Buffalo. The funding agencies had no role in study design, data collection, data analysis, interpretation or writing of the report.

Data Availability

The datasets generated and analyzed during the current study are not publicly available due to restrictions related to patient privacy, HIPAA compliance, and institutional policy governing human tissue research. De-identified data may be made available from the corresponding author upon reasonable request and with approval from the Institutional Review Board and the Jacobs School of Medicine and Biomedical Sciences.

References

1. Knopman DS, Amieva H, Petersen RC, Chételat G, Holtzman DM, Hyman BT, Nixon RA, Jones DT (2021) Alzheimer disease. Nat Rev Dis Primers 7(1):33
2. Nelson PT, Alafuzoff I, Bigio EH, Bouras C, Braak H, Cairns NJ, Castellani RJ, Crain BJ, Davies P, Del Tredici K, Duyckaerts C, Frosch MP, Haroutunian V, Hof PR, Hulette CM, Hyman BT, Iwatsubo T, Jellinger KA, Jicha GA, Kövari E, Kukull WA, Leverenz JB, Love S, Mackenzie IR, Mann DM, Masliah E, McKee AC, Montine TJ, Morris JC, Schneider JA, Sonnen JA, Thal DR, Trojanowski JQ, Troncoso JC, Wisniewski T, Woltjer RL, Beach TG (2012) Correlation of Alzheimer disease neuropathologic changes with cognitive status: a review of the literature. J Neuropathol Exp Neurol 71(5):362–381
3. Bondi MW, Edmonds EC, Salmon DP (2017) Alzheimer's disease: past, present, and future. J Int Neuropsychol Soc 23:818–831
4. Barnett R (2019) Alzheimer's disease. Lancet 393:1589
5. Korczyn AD, Grinberg LT (2024) Is Alzheimer disease a disease? Nat Rev Neurol 20(4):245–251
6. Holtzman DM, Morris JC, Goate AM (2011) Alzheimer's disease: the challenge of the second century. Sci Transl Med 3(77):77sr1
7. Therriault J, Pascoal TA, Lussier FZ, Tissot C, Chamoun M, Bezgin G, Servaes S, Benedet AL, Ashton NJ, Karikari TK, Lantero-Rodriguez J, Kunach P, Wang YT, Fernandez-Arias J, Massarweh G, Vitali P,

Soucy JP, Saha-Chaudhuri P, Blennow K, Zetterberg H, Gauthier S, Rosa-Neto P (2022) Biomarker modeling of Alzheimer's disease using PET-based Braak staging. Nat Aging 2(6):526–535

8. Therriault J, Gauthier S, Rosa-Neto P (2022) vivo tau staging in Alzheimer's disease. Aging 14(17):6842–6843
9. Hyman BT et al (2012) National Institute on Aging-Alzheimer’s Association guidelines for the neuropathologic assessment of Alzheimer’s disease. Alzheimers Dement 8:1–13
10. Montine TJ et al (2012) National Institute on Aging-Alzheimer’s Association guidelines for the neuropathologic assessment of Alzheimer’s disease: a practical approach. Acta Neuropathol 123:1–11
11. Braak H, Braak E (1991) Neuropathological stageing of Alzheimer-related changes. Acta Neuropathol 82:239–259
12. Braak H, Alafuzoff I, Arzberger T, Kretzschmar H, Tredici K (2006) Staging of Alzheimer disease-associated neurofibrillary pathology using paraffin sections and immunocytochemistry. Acta Neuropathol 112:389–404
13. Braak H, Braak E (1995) Staging of alzheimer’s disease-related neurofibrillary changes. Neurobiol Aging 16:271–278
14. Macedo AC, D.F.P.A. Durço C, Tissot J, Therriault AO, Vilela de Faria É, Aumont S, Servaes N, Rahmouni J, Fernandez-Arias Y-T, Wang FZ, Lussier A, Bieger ER, Zimmer TA, Pascoal S, Gauthier Pedro Rosa-Neto. Clinical Correlates of the PET-based Braak Staging Framework in Alzheimer's Disease. The Journal of Prevention of Alzheimer's Disease, Volume 11, Issue 2,2024,Pages 414–421.
15. Punnota RS, Vicidomini R, Passias PG, Tuil ME, Nowell J, Edison P (2026) Tau deposition can commence in multiple cortical regions in Alzheimer's trajectory before coalescing into Braak Stages. Alzheimers Dement 21(Suppl 2):e106752
16. Rani N, Alm KH, Callow DD, Pettigrew C, Soldan A, Miller M, Albert MSS, Bakker A (2025) Tau burden across Braak stages is associated with regionally specific amyloid accumulation: insights from the BIOCARD cohort. Alzheimers Dement 21(Suppl 8):e110259
17. Di Battista AM, Heinsinger NM, Rebeck GW (2016) Alzheimer's Disease Genetic Risk Factor APOE-ε4 Also Affects Normal Brain Function. Curr Alzheimer Res 13(11):1200–1207
18. Mistur R, Mosconi L, Santi SD, Guzman M, Li Y, Tsui W, de Leon MJ (2009) Current Challenges for the Early Detection of Alzheimer's Disease: Brain Imaging and CSF Studies. J Clin Neurol 5(4):153–166
19. Dang C, Wang Y, Li Q, Lu Y (2023) Neuroimaging modalities in the detection of Alzheimer's disease-associated biomarkers. Psychoradiology 3:kkad009
20. El Abiad E, Al-Kuwari A, Al-Aani U, Al Jaidah Y, Chaari A (2024) Navigating the Alzheimer’s Biomarker Landscape: A Comprehensive Analysis of Fluid-Based Diagnostics. Cells 13(22):1901
21. Liu K, Li J, Raghunathan R, Zhao H, Li X, Wong STC (2021) The Progress of Label-Free Optical Imaging in Alzheimer's Disease Screening and Diagnosis. Front Aging Neurosci 13:699024

22. Sunil N, Shikkandar A, Durai BRR, Unnathpadi R, Sankar V, Pullithadathil B (2025) Label-Free Surface-Enhanced Raman Spectroscopy Detection of Amyloid Beta on Silver Nanostructured Substrates for Alzheimer's Diagnosis. J Biophotonics 18(2):e202400314
23. Chen C, Qi J, Li Y, Li D, Wu L, Li R, Chen Q, Sun N (2024) Applications of Raman spectroscopy in the diagnosis and monitoring of neurodegenerative diseases. Front Neurosci 18:1301107
24. Ranasinghe JC, Wang Z, Huang S (2024) Unveiling brain disorders using liquid biopsy and Raman spectroscopy. Nanoscale 16(25):11879–11913
25. Ranasinghe JC, Wang Z, Huang S (2022) Raman Spectroscopy on Brain Disorders: Transition from Fundamental Research to Clinical Applications. Biosens (Basel) 13(1):27
26. Chandra A, Kumar V, Garnaik UC, Dada R, Qamar I, Goel VK, Agarwal S (2024) Unveiling the Molecular Secrets: A Comprehensive Review of Raman Spectroscopy in Biological Research. ACS Omega 9(51):50049–50063
27. Terrones O, Olazar-Intxausti J, Anso I, Lorizate M, Nieto-Garai JA, Contreras F-X (2023) Raman Spectroscopy as a Tool to Study the Pathophysiology of Brain Diseases. Int J Mol Sci 24(3):2384
28. Paraskevaidi M, Camilo LM, Morais DE, Halliwell DMA, Mann D, Allsop PL, Martin-Hirsch (2018) Martin.Raman Spectroscopy to Diagnose Alzheimer’s Disease and Dementia with Lewy Bodies in Blood. ACS Chem Neurosci 9(11):2786–2794
29. Cadusch PJ, Hlaing MM, Wade SA, McArthur SL, Stoddart PR (2013) Improved methods for fluorescence background subtraction from Raman spectra. J Raman Spectrosc 44(11):1587–1595
30. Fornasaro S, Alsamad F, Baia M, Batista de Carvalho LAE, Beleites C, Byrne HJ et al (2020) Surface enhanced Raman spectroscopy for quantitative analysis: results of a large-scale European multi-instrument interlaboratory study. Anal Chem 92(5):4053–4064
31. Gautam R, Vanga S, Ariese F, Umapathy S (2015) Review of multidimensional data processing approaches for Raman and infrared spectroscopy. EPJ Techniques Instrum 2(1):8
32. Mazet V, Carteret C, Brie D, Idier J, Humbert B (2005) Background removal from spectra by designing and minimizing a non-quadratic cost function. Chemometrics Intell Lab Syst 76(2):121–133
33. Ghazanfarpour S, Sheikhsofla A, Pourrahimi M, Sharma S, Skomra A, Sharikova A, Schwartz SA, Mahajan SD, Khmaladze A, Aalinkeel R (2025) Raman spectroscopic modality to examine therapeutic efficacy of Galectin-3 inhibitor in prostate cancer. Biochem Biophys Res Commun 757:151646
34. Wold S, Geladi P, Esbensen K, Őhman J (1987) Multi-way principal components-and PLS-analysis. J Chemometrics 1(1):41–56
35. Samuel AZ, Mukojima R, Horii S, Ando M, Egashira S, Nakashima T et al (2021) On selecting a suitable spectral matching method for automated analytical applications of Raman spectroscopy. ACS Omega 6(3):2060–2065
36. Szalontai B, Debreczeny M, Fintor K, Bagyinka C (2020) SVD-clustering, a general image-analyzing method explained and demonstrated on model and Raman micro-spectroscopic maps. Sci Rep 10(1):4238

37. Tubbesing K, Khoo TC, Bahreini Jangjoo S, Sharikova A, Barroso M, Khmaladze A (2021) Iron-binding cellular profile of transferrin using label-free Raman hyperspectral imaging and singular value decomposition (SVD). Free Radic Biol Med. 2021, Volume 169,Pages 416–424,ISSN 0891–5849
38. Gurian E, Di Silvestre A, Mitri E, Pascut D, Tiribelli C, Giuffrè M, Crocè LS, Sergo V, Bonifacio A (2021) Repeated double cross-validation applied to the PCA-LDA classification of SERS spectra: a case study with serum samples from hepatocellular carcinoma patients. Anal Bioanal Chem 413(5):1303–1312. 10.1007/s00216-020-03093-7
39. Schmittgen TD, Livak KJ (2008) Analyzing real-time PCR data by the comparative C(T) method. Nat Protoc 3(6):1101–1108
40. Livak KJ, Schmittgen TD Analysis of Relative Gene Expression Data Using Real-Time Quantitative PCR and the 2 – ΔΔCT Method. Methods, 25, Issue 4,2001,Pages 402–408
41. Xu Y, Pan X, Li H, Cao Q, Xu F, Zhang J (2023) Accuracy of Raman spectroscopy in the diagnosis of Alzheimer's disease. Front Psychiatry 14:1112615
42. Pérez-Elvira R, Oltra-Cucarella J, Agudo Juan M, Polo-Ferrero L, Juárez-Vela R, Bosch-Bayard J, Quintana Díaz M, de la Cruz J (2025) Salgado Ruíz A. The Vibrational Signature of Alzheimer's Disease: A Computational Approach Based on Sonification, Laser Projection, and Computer Vision Analysis. Biomimetics 10(12):792
43. Depciuch J, Zawlik I, Skrzypa M, Pająk J, Potocka N, Łach K, Bartosik-Psujek H, Koziorowska A, Kaznowska E, Cebulski J (2019) FTIR Spectroscopy of Cerebrospinal Fluid Reveals Variations in the Lipid: Protein Ratio at Different Stages of Alzheimer's Disease. J Alzheimers Dis 68(1):281–293
44. Röhr D, Helfrich M, Höring M, Großerüschkamp F, Liebisch G, Gerwert K (2025) Unsaturated Fatty Acids Are Decreased in Aβ Plaques in Alzheimer's Disease. J Neurochem 169(1):e16306
45. Chew H, Solomon VA, Fonteh AN (2020) Involvement of Lipids in Alzheimer's Disease Pathology and Potential Therapies. Front Physiol 11:598
46. Brüggemann J, Chekmeneva M, Wolter M, Jacob CR (2023) Structural Dependence of Extended Amide III Vibrations in Two-Dimensional Infrared Spectra. J Phys Chem Lett 14(41):9257–9264
47. Tóth G, Watts CR, Murphy RF, Lovas S (2001) Significance of aromatic-backbone amide interactions in protein structure. Proteins 43(4):373–381
48. Ganim Z, Chung HS, Smith AW, Deflores LP, Jones KC, Tokmakoff A (2008) Amide I two-dimensional infrared spectroscopy of proteins. Acc Chem Res 41(3):432–441
49. Yin F Lipid metabolism and Alzheimer's disease: clinical evidence, mechanistic link and therapeutic promise. FEBS J Volume290, Issue6, March 2023, Pages 1420–1453
50. Cioffi F, Adam RHI, Broersen K (2019) Molecular Mechanisms and Genetics of Oxidative Stress in Alzheimer's Disease. J Alzheimers Dis 72(4):981–1017
51. Lochocki B, Boon BDC, Verheul SR, Zada L, Hoozemans JJM, Ariese F, de Boer JF (2021) Multimodal, label-free fluorescence and Raman imaging of amyloid deposits in snap-frozen Alzheimer's disease human brain tissue. Commun Biol 4(1):474

52. Ribarič S (2023) Detecting Early Cognitive Decline in Alzheimer's Disease with Brain Synaptic Structural and Functional Evaluation. Biomedicines 11(2):355
53. Tenchov R, Sasso JM, Zhou QA Alzheimer's Disease: Exploring the Landscape of Cognitive Decline. ACS Chem Neurosci 2024 15 (21), 3800–3827
54. Tsoi PS, Quan MD, Ferreon JC, Ferreon ACM (2023) Aggregation of Disordered Proteins Associated with Neurodegeneration. Int J Mol Sci 24(4):3380
55. Tramutola A, Lanzillotta C, Perluigi M, Butterfield DA (2017) Oxidative stress, protein modification and Alzheimer disease. Brain Res Bull 133:88–96
56. Cheignon C, Tomas M, Bonnefont-Rousselot D, Faller P, Hureau C, Collin F (2018) Oxidative stress and the amyloid beta peptide in Alzheimer's disease. Redox Biol 14:450–464
57. Thangaleela S, Ali A, Tandoro Y, Wang C-K (2026) Shared Neuroinflammatory Mechanisms Across Dementia Types: An Integrative Review. Int J Mol Sci 27(1):179. https://doi.org/10.3390/ijms27010179
58. Keller JN (2006) Interplay between oxidative damage, protein synthesis, and protein degradation in Alzheimer's disease. J Biomed Biotechnol 2006(3):12129
59. Mrđenović D, Combes BF, Ni R, Zenobi R, Kumar N (2024) Probing Chemical Complexity of Amyloid Plaques in Alzheimer's Disease Mice using Hyperspectral Raman Imaging. ACS Chem Neurosci 15(1):78–85
60. de Dios C, Bartolessis I, Roca-Agujetas V, Barbero-Camps E, Mari M, Morales A, Colell A (2019) Oxidative inactivation of amyloid beta-degrading proteases by cholesterol-enhanced mitochondrial stress. Redox Biol 26:101283
61. Butterfield DA, Swomley AM, Sultana R (2013) Amyloid β-peptide (1–42)-induced oxidative stress in Alzheimer disease: importance in disease pathogenesis and progression. Antioxid Redox Signal 19(8):823–835
62. Drolle E, Negoda A, Hammond K, Pavlov E, Leonenko Z (2017) Changes in lipid membranes may trigger amyloid toxicity in Alzheimer's disease. PLoS ONE 12(8):e0182194
63. Igarashi M, Ma K, Gao F, Kim HW, Rapoport SI, Rao JS (2011) Disturbed choline plasmalogen and phospholipid fatty acid concentrations in Alzheimer's disease prefrontal cortex. J Alzheimers Dis 24(3):507–517
64. Wang S, Zhang W, Fu P, Zhong Y, Piatkevich KD, Zhang D, Lee HJ (2024) Structural diversity of Alzheimer-related protein aggregations revealed using photothermal ratio-metric micro-spectroscopy. Biomed Opt Express 15(12):6768–6782
65. Cukalevski R, Boland B, Frohm B, Thulin E, Walsh D, Linse S (2012) Role of aromatic side chains in amyloid β-protein aggregation. ACS Chem Neurosci 3(12):1008–1016
66. Kong J, Yu S (2007) Fourier Transform Infrared Spectroscopic Analysis of Protein Secondary Structures. Acta biochimica et biophysica Sinica. 39. 549 – 59

67. Paulus A, Engdahl A, Yang Y, Boza-Serrano A, Bachiller S, Torres-Garcia L, Svanbergsson A, Garcia MG, Gouras GK, Li J-Y et al (2021) Amyloid Structural Changes Studied by Infrared Microspectroscopy in Bigenic Cellular Models of Alzheimer's Disease. Int J Mol Sci 22(7):3430
68. Malek-Ahmadi M, Perez SE, Chen K, Mufson EJ (2020) Braak Stage, Cerebral Amyloid Angiopathy, and Cognitive Decline in Early Alzheimer's Disease. J Alzheimers Dis 74(1):189–197
69. Pericak-Vance MA, Nam Y, DeRosa BA, Ramirez AM, Ayele BA, Whitehead PG, Adams LD, Golightly CG, Starks TD, Laverde-Paz J, Cukier HN, Akinyemi R, Sarfo F, Akpalu A, Cuccaro ML, Williams S, Caban-Holt A, Reitz C, Haines JL, Goldie BS, Rajabli F, Dykxhoorn DM, Young JI, Vance JM (2025) Disrupted Lipid Homeostasis as a Pathogenic Mechanism in ABCA7-Associated Alzheimers Disease Risk. bioRxiv [Preprint]. Sep 7:2025.09.03.673792
70. Akram A, Schmeidler J, Katsel P, Hof PR, Haroutunian V (2010) Increased expression of cholesterol transporter ABCA1 is highly correlated with severity of dementia in AD hippocampus. Brain Res 1318:167–177
71. Jihong Kang S, Rivest (October 2012) Lipid Metabolism and Neuroinflammation in Alzheimer's Disease: A Role for Liver X Receptors, Endocrine Reviews. 33(5):1
72. Ju Y, Li S, Kong X, Zhao Q (2024) Exploring fatty acid metabolism in Alzheimer's disease: the key role of CPT1A. Sci Rep 14(1):31483
73. Liang K (2023) Mitochondrial CPT1A: Insights into structure, function, and basis for drug development. Front. Pharmacol. 2023; 14:1160440. 10.3389/fphar.2023.1160440
74. Lin Y, Wang Y, Li PF, PPARα (2022) An emerging target of metabolic syndrome, neurodegenerative and cardiovascular diseases. Front Endocrinol (Lausanne) 13:1074911. 10.3389/fendo.2022.1074911
75. Eberlé D, Hegarty B, Bossard P, Ferré P, Foufelle F (2004) SREBP transcription factors: master regulators of lipid homeostasis. Biochimie 86(11):839–848. 10.1016/j.biochi.2004.09.018
76. Crack P, Cimdins K, Ali U et al (2006) Lack of glutathione peroxidase-1 exacerbates Aβ-mediated neurotoxicity in cortical neurons. J Neural Transm 113:645–657. https://doi.org/10.1007/s00702-005-0352-y
77. Fakhoury M (2018) Microglia and Astrocytes in Alzheimer's Disease: Implications for Therapy. Curr Neuropharmacol 16(5):508–518. 10.2174/1570159X15666170720095240
78. Deng Q, Wu C, Parker E, Liu TC, Duan R, Yang L (2024) Microglia and Astrocytes in Alzheimer's Disease: Significance and Summary of Recent Advances. Aging Dis 15(4):1537–1564. 10.14336/AD.2023.0907
79. Perluigi M, Di Domenico F, Butterfield DA (2024) Oxidative damage in neurodegeneration: roles in the pathogenesis and progression of Alzheimer disease. Physiol Rev 104(1):103–197. 10.1152/physrev.00030.2022
80. Jurcău MC, Andronie-Cioara FL, Jurcău A, Marcu F, Ţiț DM, Pașcalău N, Nistor-Cseppentö DC (2022) The Link between Oxidative Stress, Mitochondrial Dysfunction and Neuroinflammation in the

Pathophysiology of Alzheimer's Disease: Therapeutic Implications and Future Perspectives. Antioxid (Basel) 11(11):2167. 10.3390/antiox11112167

81. Jurcău MC, Andronie-Cioara FL, Jurcău A, Marcu F, Ţiț DM, Pașcalău N, Nistor-Cseppentö DC (2022) The Link between Oxidative Stress, Mitochondrial Dysfunction and Neuroinflammation in the Pathophysiology of Alzheimer's Disease: Therapeutic Implications and Future Perspectives. Antioxid (Basel) 11(11):2167. 10.3390/antiox11112167
82. Zheng Q, Xin, Wang (2025) Alzheimer’s disease: insights into pathology, molecular mechanisms, and therapy, Protein & Cell, Volume 16, Issue 2, February Pages 83–120. https://doi.org/10.1093/procel/pwae026
83. Spangenberg EE, Green KN (2017) Inflammation in Alzheimer's disease: Lessons learned from microglia-depletion models. Brain Behav Immun 61:1–11. 10.1016/j.bbi.2016.07.003
84. Ivanova AV, Kutuzova AD, Kuzmichev IA, Abakumov MA (2025) Alzheimer’s Disease: From Molecular Mechanisms to Promising Therapeutic Strategies. Int J Mol Sci 26(19):9444. https://doi.org/10.3390/ijms26199444

Figures

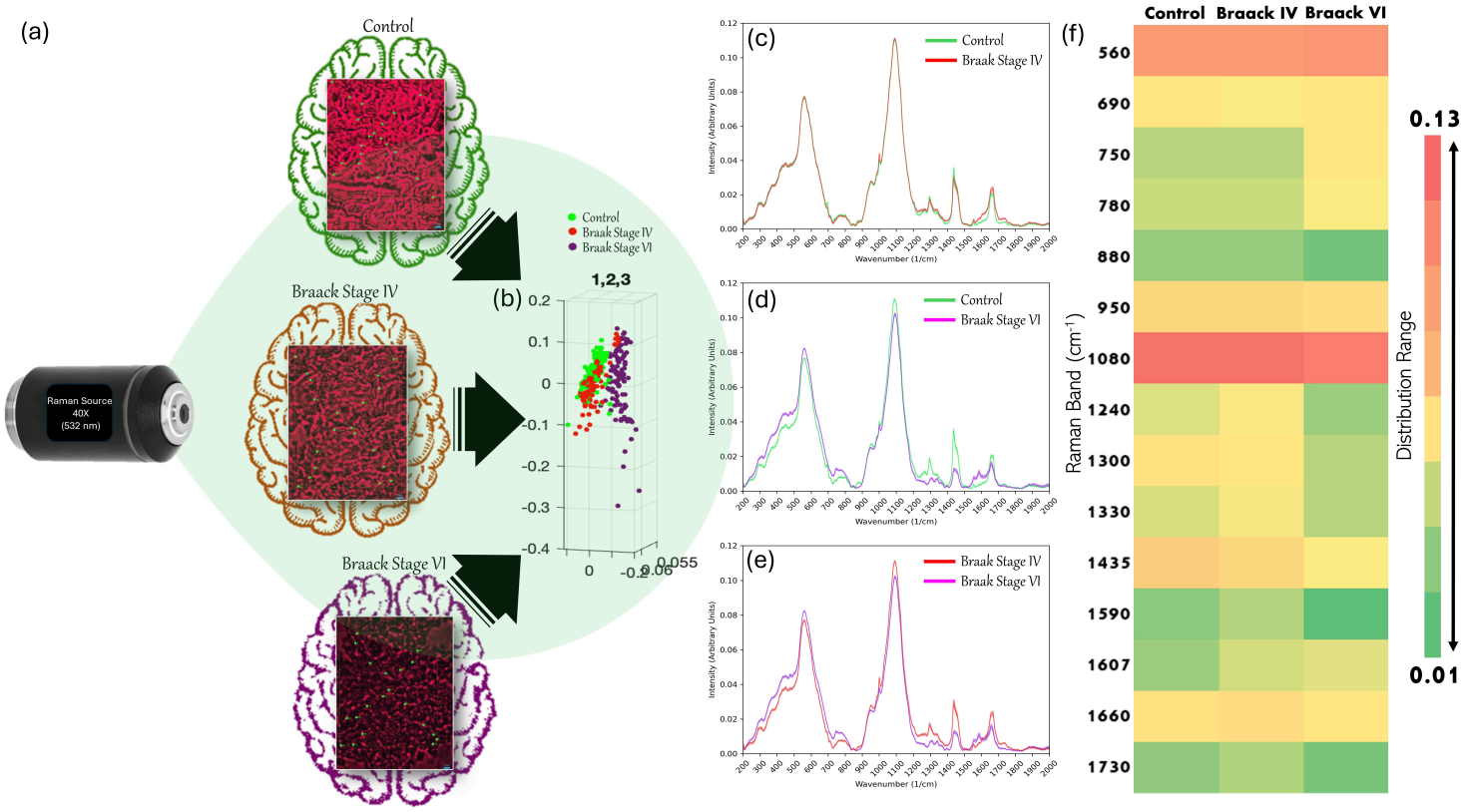

Figure 1

(a) Schematic of the Raman spectroscopy experiment design; (b) Raman Spectrum baseline subtracted, normalized average spectra from the 3 groups with 95 % confidence intervals. (b) Raman analysis

showing three coordinate comparison for AD samples Blaak stage IV, Braack stage VI and control groups; (c) Raman analysis showing comparative signal shifts in Raman spectra for control samples vs Braak IV AD samples; (d) Raman analysis showing comparative signal shifts in Raman spectra for control samples vs Braak VI AD samples; (e) Raman analysis showing comparative signal shifts in Raman spectra for Braak IV vs Braak VI AD samples. (f) Distribution range of Raman spectral bands across Control, Braack IV, and Braack VI conditions. Heatmap depicting the distribution range of Raman spectral bands (560–1730 cm^{-1}) under three experimental conditions: Control, Braack IV, and Braack VI. The y-axis represents Raman shifts, while the x-axis categorizes the conditions. The color gradient indicates the extent of distribution, with red denoting higher variability (up to 0.13) and green indicating lower variability (down to 0.01). This visualization highlights molecular heterogeneity associated with progressive Braack staging.

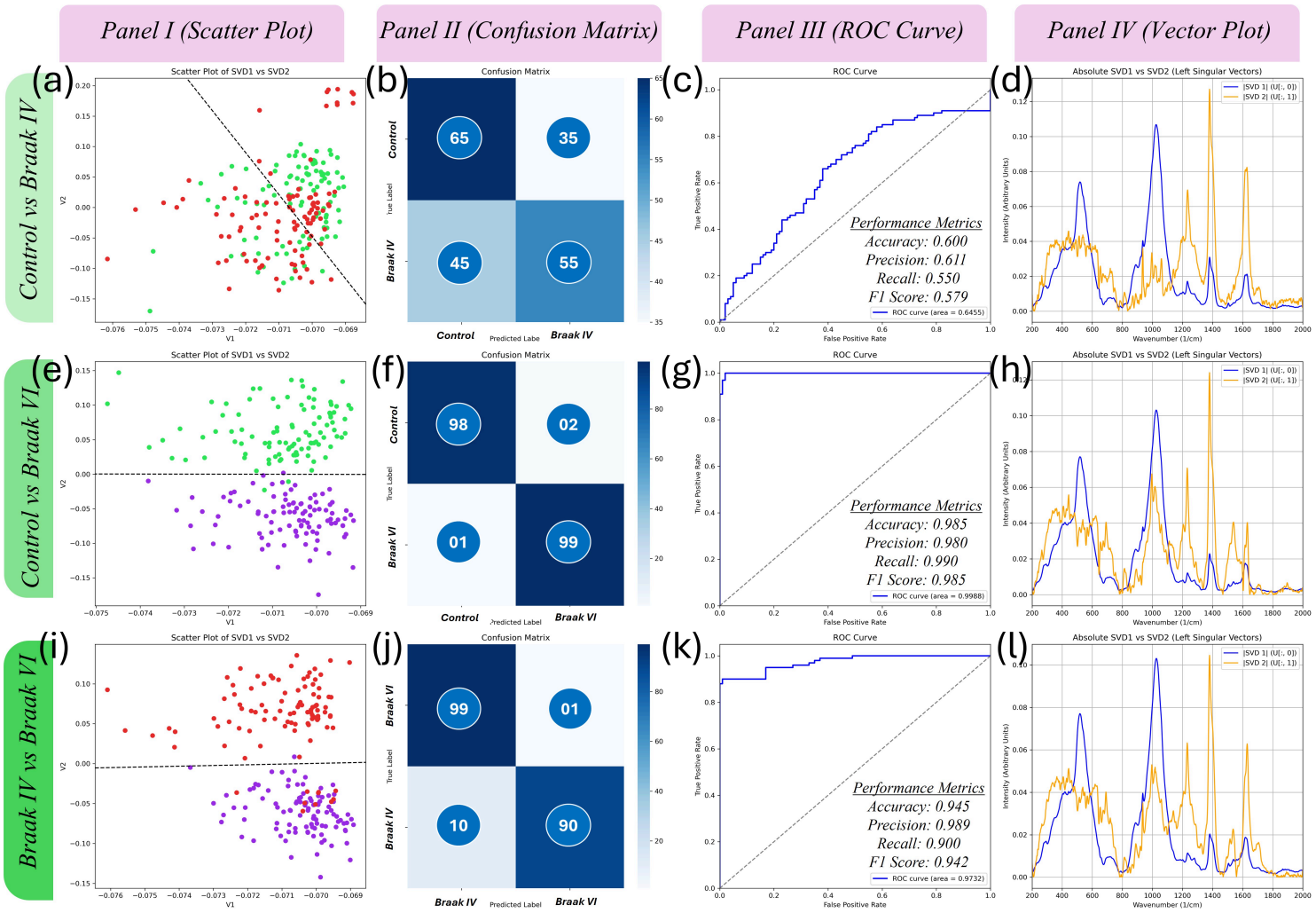

Figure 2

SVD and LDA results demonstrate clear separation of Raman spectral clusters corresponding AD samples vs Controls and between Controls vs Braak IV and Control vs Braak VI. Fig 2 (a,e,i) shows Scatter Plots between Control vs Braak IV, Control vs Braak VI, and Braak IV vs Braak VI respectively. Fig 2 (b,f,j) shows the accompanying confusion matrices illustrate classification performance for each sample group, highlighting the accuracy of spectral differentiation across AD Stages. ROC curve analysis

demonstrated clear classification performance across groups, with accuracy/precision/F1 scores of 0.60/0.611/0.579 for control vs Braak IV (Fig. 2c), 0.985/0.980/0.985 for control vs Braak VI (Fig. 2g), and 0.945/0.989/0.942 for Braak IV vs Braak VI (Fig. 2k). Corresponding spectral comparisons (Fig. 2d,h,l) illustrate the key Raman signal shifts distinguishing each pair of sample groups.

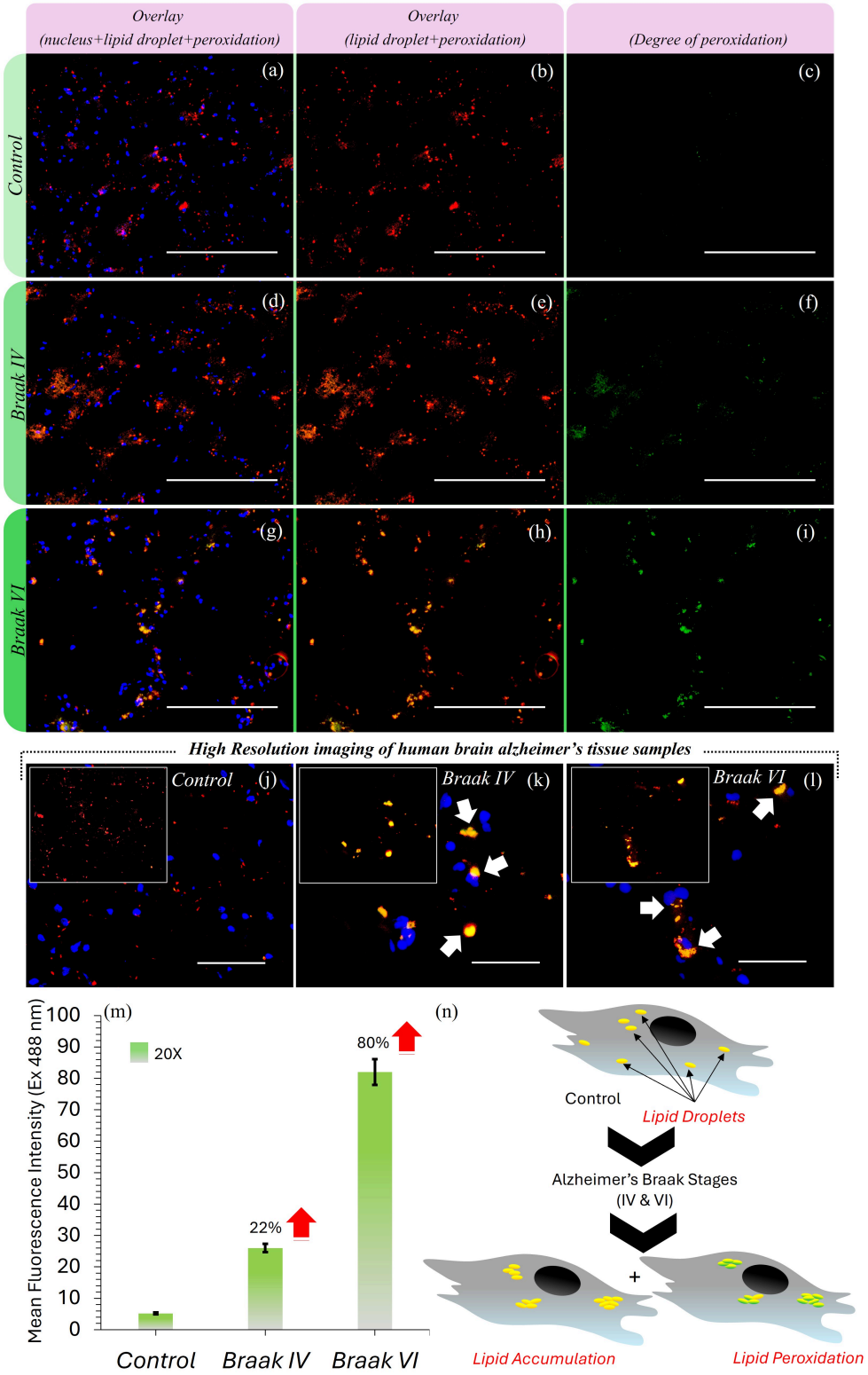

Figure 3

Increased lipid peroxidation and lipid aggregation in Alzheimer's disease (AD) brain tissue. Representative confocal images of BODIPY™ 581/591 C11 staining show predominantly reduced (red) fluorescence in control sections and a marked shift toward oxidized (green) signal in AD tissue, consistent with elevated lipid peroxidation. Quantified green-to-red ratios demonstrate higher lipid oxidation in AD, with Braak VI samples exhibiting greater peroxidation and more abundant punctate lipid aggregates than Braak IV. Panels (a–j) show 20× images (scale bar: 400 μm); panels (j–l) show 40× images (scale bar: 100 μm). AD sections exhibited a pronounced shift from reduced (red) to oxidized (green) fluorescence, indicating increased peroxidation of lipid droplets, whereas control samples showed predominantly red signal. Quantification of the green-to-red fluorescence ratio (Fig. 3m) confirms significantly higher lipid oxidation in AD samples. Fig. 3n, shows a schematic highlighting increased lipid peroxidation and lipid aggregation in Braak IV ($p<0.05$) and Braak VI AD ($p<0.01$) brain tissue compared to the controls, supporting a link between oxidative lipid damage and late-stage AD neurodegeneration.

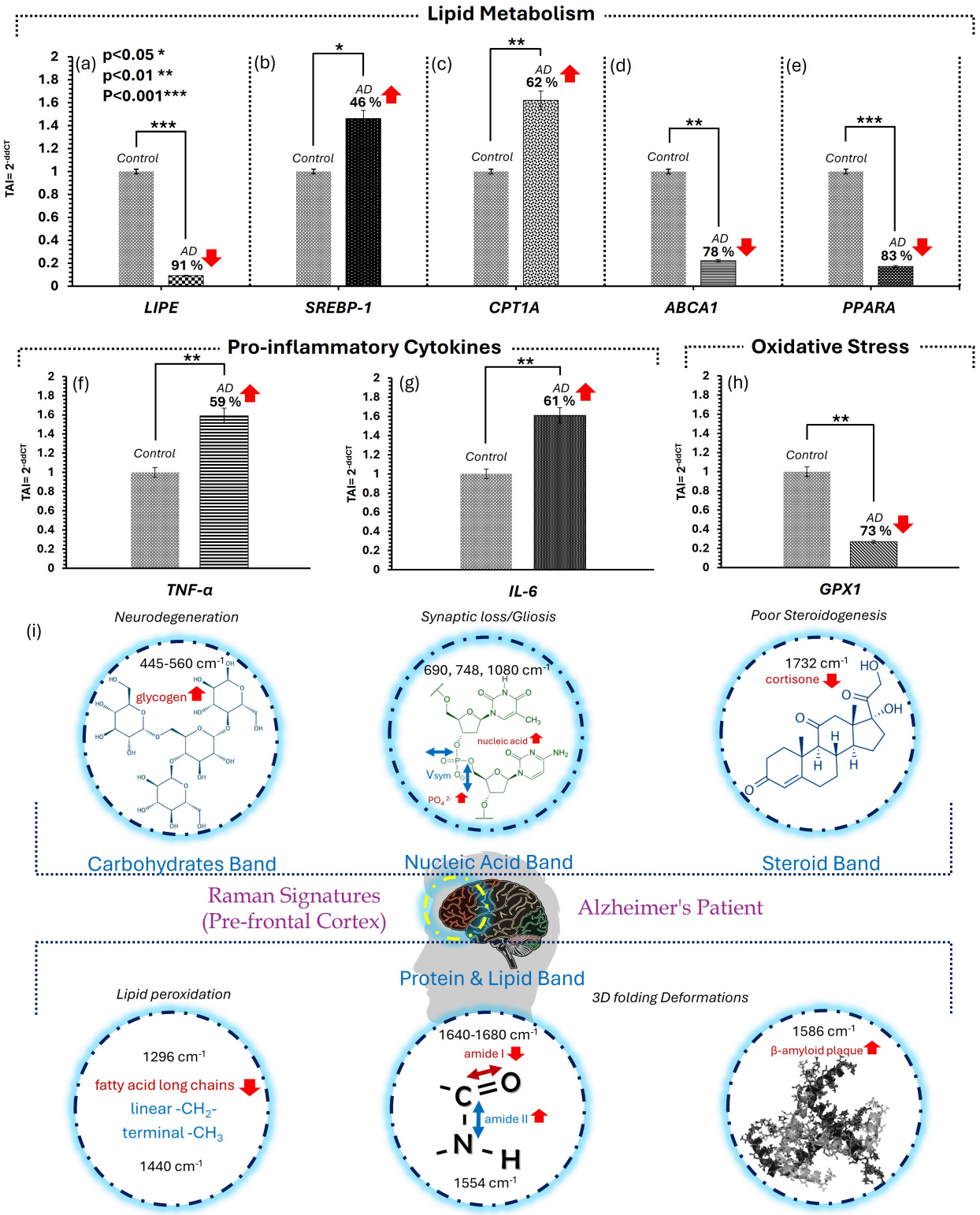

Figure 4

Gene expression analysis in AD brain tissue samples and normal controls

(a-e) Genes involved in Lipid metabolism LIPE, SREBP-1, CPT1A, ABCA1 and PPARA (f-g) Genes for proinflammatory Cytokines, TNF-α & IL-6; (h Oxidative stress mitigator gene GPX1. (i)- Schematic of key Raman spectral bands modulated in pre-frontal cortex Brain tissue from AD patients and their specific

biochemical relevance representing carbohydrates, nucleic acids, steroids, Protein & Lipids and their potential relevance to AD pathophysiology namely neurodegeneration, Synaptic loss/Gliosis, Poor Streoidogenesis, alter Lipid peroxidation, and protein folding deformation (Amyloid beta plaques).

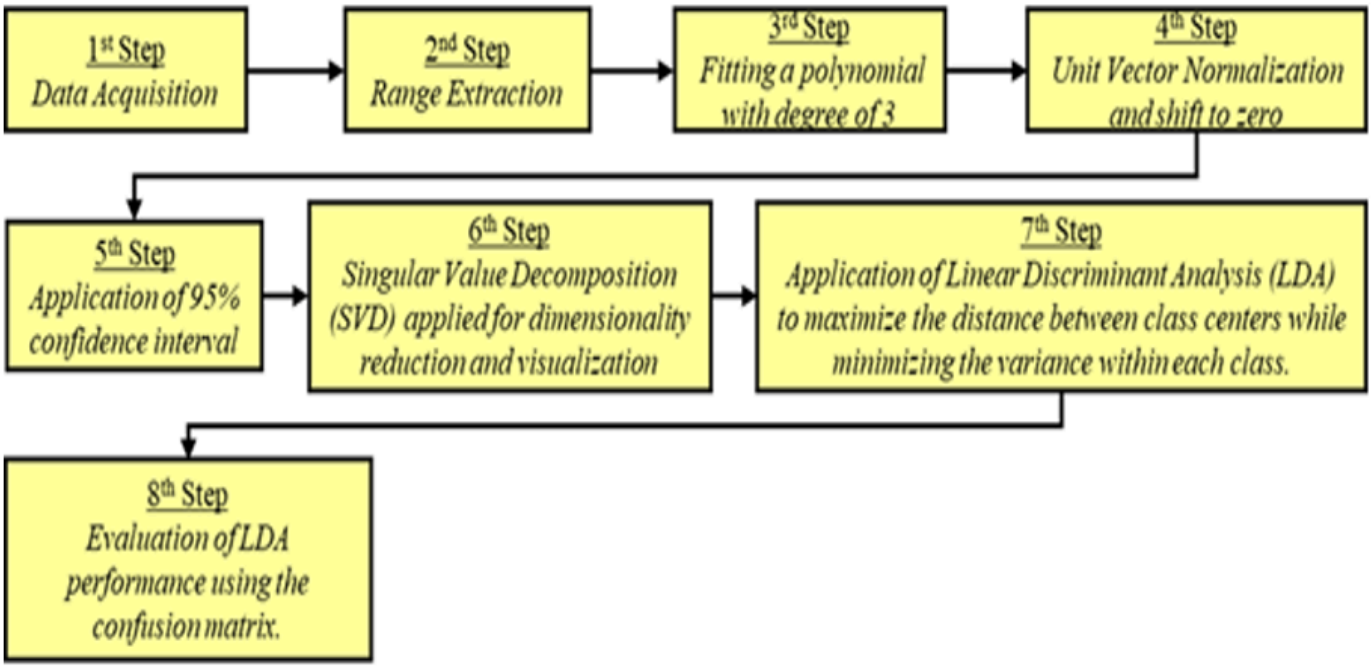

Figure 5

Unnumbered image in the Materials & Methods section.